Proton beam induced dynamics of tungsten granules

O. Caretta, P. Loveridge, J. O'Dell, T. Davenne, M. Fitton, A. Atherton, and C. Densham
STFC Rutherford Appleton Laboratory, Didcot OX11 0QX, United Kingdom

N. Charitonidis, I. Efthymiopoulos, A. Fabich, M. Guinchard, L. J. Lacny, and B. Lindstrom
CERN, 1211 Geneva 23, Switzerland

(Received 21 March 2017; revised manuscript received 1 February 2018; published 29 March 2018)

This paper reports the results from single-pulse experiments of a 440 GeV/c proton beam interacting with granular tungsten samples in both vacuum and helium environments. Remote high-speed photography and laser Doppler vibrometry were used to observe the effect of the beam on the sample grains. The majority of the results were derived from a trough containing ~45 μm diameter spheres (not compacted) reset between experiments to maintain the same initial conditions. Experiments were also carried out on other open and contained samples for the purposes of comparison both with the 45 μm grain results and with a previous experiment carried out with sub-250 μm mixed crystalline tungsten powder in helium [Phys. Rev. ST Accel. Beams **17**, 101005 (2014)]. The experiments demonstrate that a greater dynamic response is produced in a vacuum than in a helium environment and in smaller grains compared with larger grains. The examination of the dynamics of the grains after a beam impact leads to the hypothesis that the grain response is primarily the result of a charge interaction of the proton beam with the granular medium.

DOI: 10.1103/PhysRevAccelBeams.21.033401

I. INTRODUCTION

Packed beds and granular flows are of interest as a potential high-Z target technology for future high-energy physics and nuclear facilities [1–3] as an alternative to liquid metals in contained or open jet configurations [4–9]. Like liquid metals, granular targets permit efficient in-line recirculation cooling after an interaction with the beam while limiting thermal expansion stresses to small confines. In order to evaluate the effects of a proton beam on granules, an initial experiment was performed in 2012 at the HiRadMat facility at CERN [10], where a static tungsten powder sample of sub-250 μm crystalline grains was exposed to a 440 GeV/c, c.2 mm rms radius, 7 μs duration proton beam pulse [11,12]. The 2012 experiment revealed that tungsten powder, immersed in a helium environment initially at rest in a free surface trough, is lifted when shot with more than 4.6×10^{10} protons on target (POT). Three mechanisms were hypothesized acting on the powder: gas expansion driven aerodynamic drag, thermal expansion driven stress propagation between grains, and intergranular repulsion due to beam induced electrostatic or electromagnetic effects [13]. This paper reports results from a follow-on experiment performed in 2015 at the HiRadMat facility, to further investigate this effect and to gain an understanding of the physical mechanisms of the powder response to the beam. In this experiment, samples of different grain sizes were exposed to the beam, initially in a vacuum and then in a helium atmosphere. In both experiments, remote high-speed video (HSV) was used to record the dynamics of free surface samples, while laser Doppler vibrometry (LDV) was used to study the stress propagation from packed bed samples to the container walls.

II. EXPERIMENTAL SETUP

The powder irradiation experiment was performed over three sessions in June and July 2015 at the HiRadMat facility at CERN. For the experiments a powder containment rig was installed in the TNC (Tunnel Neutrino Chamber) tunnel, whereas the HSV and LDV instrumentation was placed in the adjacent TT61 tunnel.

The powder rig was installed on a remotely operated cradle described in Ref. [11] which was used to lift the equipment into surveyed kinematic mounts fixed in the TNC tunnel. A remotely operated lift stand on the cradle permitted the sample box to be moved into the beam to conduct the experiments and, in addition to the beam line magnets, allowed the beam height to be adjusted with respect to the surface of the powder samples.

As shown in the schematic layout in Fig. 1, an arrangement with three optical mirrors was used to project the side

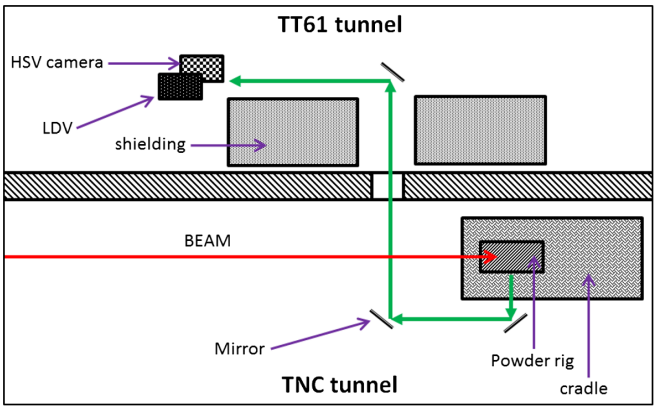

FIG. 1. Plan view of the experiment and instrumentation in the experimental tunnels.

view of the powder container back to a HSV and a LDV, which were installed behind a shielding block in the adjacent tunnel. A feedthrough with an optical window maintained separate ventilation between the TNC and the TT61 tunnels while granting an optical path for the image. One of the mirrors was mounted on a remotely operated linear stage, which allowed the LDV focus to be moved between different sample containers.

Figure 1 shows the layout of the TNC and TT61 tunnels, the powder rig on the cradle, a set of three mirrors with the optical path, the HSV camera, and the LDV with their shielding arrangement. As highlighted by the green lines in Fig. 1, the image from the rig was projected via the three mirrors back to the HSV camera and LDV, which were in the adjacent tunnel.

The powder rig consisted of a set of two nested aluminum enclosures to provide double containment to the irradiated tungsten powder. Three free surface tungsten powder samples and three enclosed packed bed-style samples were loaded into the inner container. Figure 2 shows the powder samples (in red and yellow) housed within two concentric containers with the optical view ports (light blue) used to acquire the HSV and LDV data and the titanium beam entry and exit windows (in okra color).

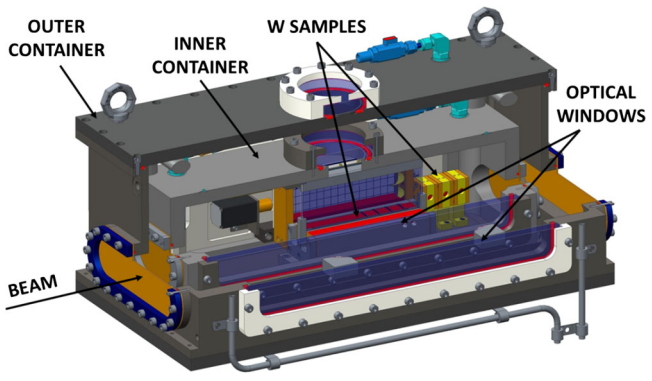

FIG. 2. Section drawing of the tungsten powder rig.

The inner container was evacuated before installation in the tunnel to approximately 20 mbar absolute pressure, allowing the initial experiments to be performed in a mechanical vacuum. The outer container was initially filled with helium at 1.5 bar absolute pressure. Eventually, a remotely operated valve was used to equalize the pressure between the outer container and the inner container to 1.15 bar absolute pressure so that some of the experiments could be repeated in a helium atmosphere.

Figure 3 illustrates in the plan view the arrangement of the powder samples within the inner containment box. A horizontal translation stage allowed the powder rig to be shifted laterally to select the required sample to interact with the beam. The translation was monitored by a linear displacement voltage transducer with a precision of $\pm 100\ \mu$m and confirmed by three mechanical position switches. The first trough (bottom in Fig. 3) was loaded with 60 mesh (i.e., smaller than 250 μm) crystalline powder, reproducing the setup of the 2011 experiment. The middle trough was loaded with a sequence of spherical samples of different sizes (see Table I). Each size distribution was separated from its neighbor by a double titanium septum (i.e., two 25 μm titanium foils separated by a 1 mm u-shaped aluminum spacer) intended to prevent stress propagation from one sample to the next. The last trough (top in Fig. 3) was loaded with W-45 (see Table I) and completely enclosed sideways by two glass panes, longitudinally by titanium windows and at the top by a flexible Kapton seal. The glass panes were spaced 20 mm apart, the trough was 160 mm long, and the powder was infilled to a height of ~22 mm. This trough was lined up with three enclosed packed bed samples. These samples were completely enclosed except from a small top venting orifice for equalization of the pressure. A horizontal section of the packed bed samples (i.e., missing the lid) is shown in yellow and red in Fig. 3 (labeled 3, 4, and 5). Here the white circled numbers 1–5 identify the different targets aimed at by the LDV.

The large optical window, the glass separation pane between the multisize trough and the crystalline trough, and

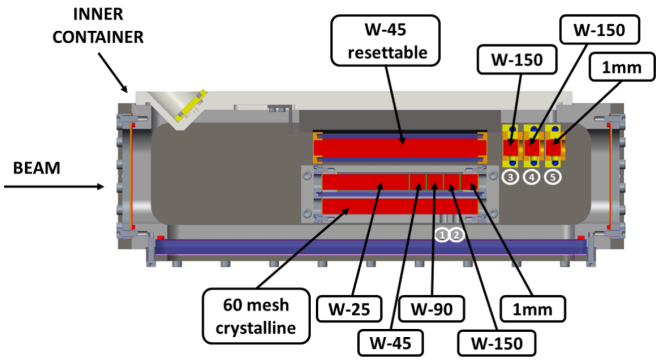

FIG. 3. Plan cross section view of the free surface tungsten troughs and packed bed samples.

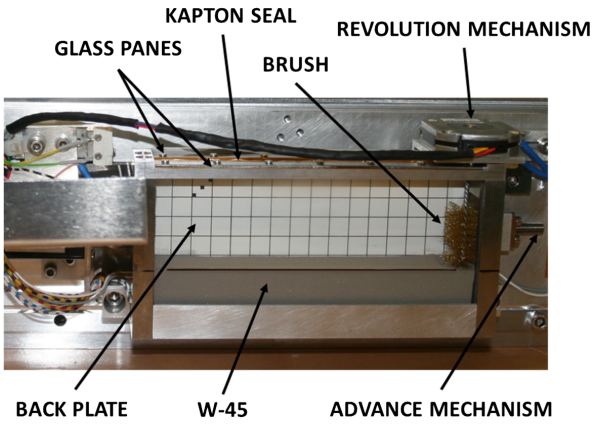

FIG. 4. Resettable trough before assembly in the rig.

the glass walls of the resettable trough are shown in blue in Fig. 3. The large windows on the outer and inner containers were made from toughened soda-lime glass, whereas the small glass panes close to the samples were made of fused silica in order to reduce darkening due to radiation damage.

The trough containing the W-45 powder was contained within two glass panes, and a flexible Kapton deflector at the top prevented it from escaping during the lifts. The black level line in the figure was scored to facilitate the powder filling. A brass wire brush was installed inside the containment of this sample and served a double purpose: (a) to reset the powder level in the trough in between pulses and (b) to clean the glass panes from possible dust residues after the powder lifts. The brush was remotely operated and rotated on its axis while advancing along the sample trough. The position of the brush at a given moment could be ascertained with the high-speed video camera as well as with limit switches. The sweeping brush made it possible to return the powder in the trough to a standard initial condition so as to perform multiple sequential experiments from a known baseline. A white painted reference aluminum plate was attached to the back glass pane, scored with a 10 mm grid. The setup is shown in detail in Fig. 4.

The specification of the six different tungsten granular samples, loaded in the rig as shown in Fig. 3, is described in Table I. The Tekmat material consisted of plasma spheroidized tungsten. Figure 5 (left) shows a micrograph of the spheroidized W-45 powder which was loaded in the resettable trough. The 60 mesh crystalline tungsten was

TABLE I. Powder samples used for the experiment.

Name	Size range	Supplier
W-25	$5 < d < 25\ \mu m$	www.tekna.com
W-45	$15 < d < 45\ \mu m$	www.tekna.com
W-90	$45 < d < 90\ \mu m$	www.tekna.com
W-150	$75 < d < 150\ \mu m$	www.tekna.com
60 mesh crystalline	$0 < d < 250\ \mu m$	Wilbury Metals Ltd.
Large beads	1.05 mm	IMPCAS

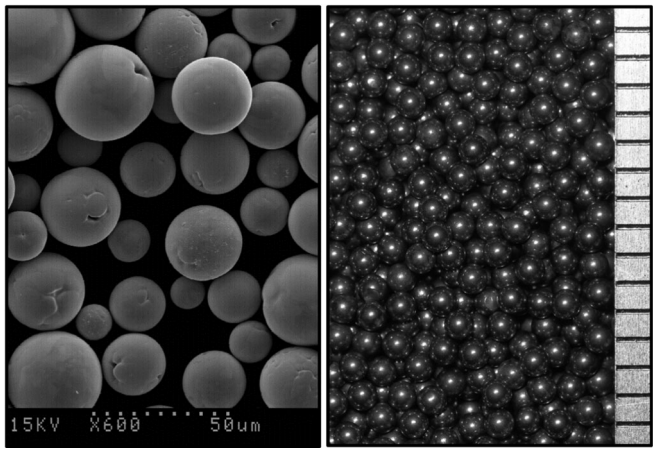

FIG. 5. Tekmat W-45 plasma spheroidised tungsten (left, SEM picture) and IMPCAS 1 mm spheres (right).

extracted from the same batch as that used in the 2011 experiment [11]. Figure 5 (right) shows a picture of the large 1.05 mm tungsten beads supplied by Institute of Modern Physics, Chinese Academy of Sciences (IMPCAS) and used for the packed bed sample.

The material was loaded in the open top troughs and packed bed samples and gently tapped but not compressed, yielding an estimated bulk density of approximately 9 g/cc.

III. REMOTE HIGH-SPEED PHOTOGRAPHY

A monochrome Redlake high-speed video camera model MotionXtra HG-100k was used to record the powder's response to the beam. A frame rate of 1 kHz was chosen based on the recorded powder disruption speeds observed in the first experiment. The camera was set up behind concrete shielding and had an optical path of approximately 10 m from the target. The camera was coupled with an aperture regulation adaptor (Fotodiox Pro Lens Mount Adapter—Nikon G Mount Lenses to C-Mount with lens aperture control), a 2× Kenko teleconverter, and a Tamron SP 150–600 mm F/5-6.3 Di VC USD optical lens. The effective field of view was approximately 160 mm wide by 60 mm high, resulting in a pixel resolution of ~106 μm. Focusing on the target while minimizing optical aberrations and light reflections was made challenging by the 10 m distance, three mirrors, and six glass containment panes on the optical path.

For the HSV, the rig was lit up with an arrangement of 12 LED clusters ILR-ON10-ULWH-SC201, each consisting of 10 OSRAM OSLON LEDs. The clusters were supplied with 700 mA, producing a nominal luminous flux of 1760 lms for each cluster, i.e., a total of 21120 lumens for the whole rig. The clusters were installed on a C-shaped aluminum heat sink in the outer containment box, running along the periphery of the field of view at the front, the top, and the back of the troughs. The heat sink was fastened to the aluminum outer container, which was actively water

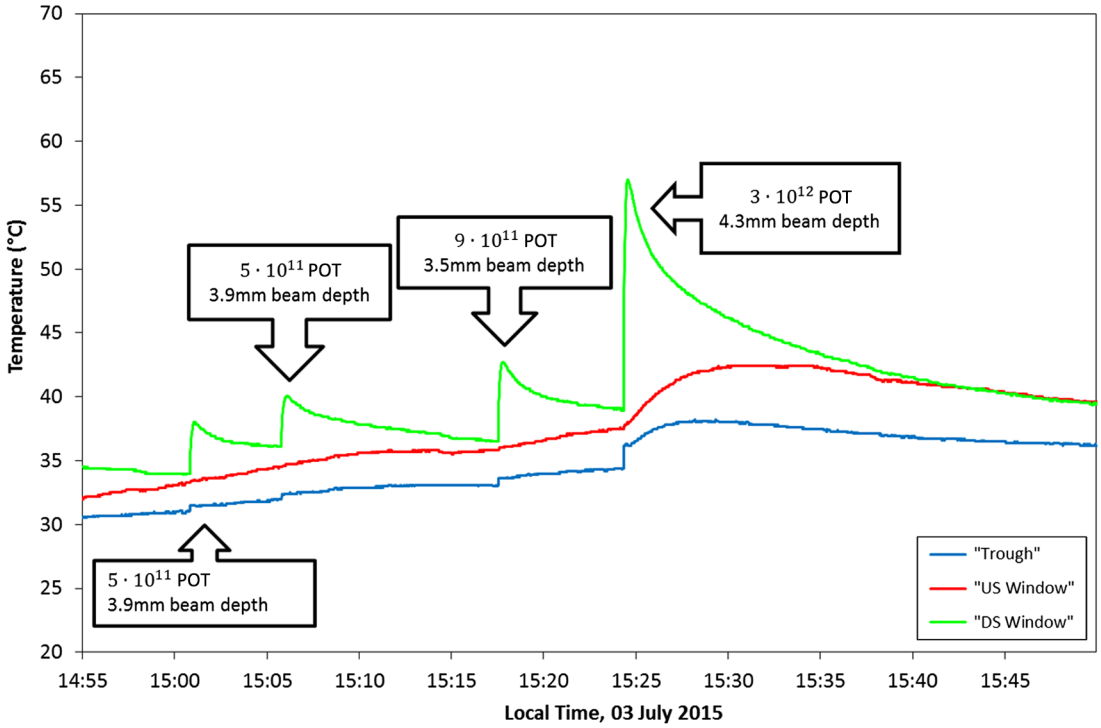

FIG. 6. Record of powder container temperature jumps on day 3 with the nominal depth of the beam below the powder surface indicated (US, upstream; DS, downstream).

cooled during the experiments so that the LEDs operated at around 40 °C.

Beam induced stress propagation through the samples was measured using a Polytec RSV150 vibrometer, following the same optical path as the high-speed camera. The instrument was set to a sampling rate of ∼205 kHz and a sensitivity of 12.25 mm/s/V for velocity and 12.25 μm/V for displacement. A beam trigger signal was recorded together with the LDV signal to measure the speed of the stress propagation (i.e., the sound speed) in the granular media.

The LDV was aimed in turn at the five different target samples identified by the white numbers in Fig. 3. LDV targets 1 and 2 were 25 μm thick, 8 mm diameter titanium diaphragms, with target 1 directly in contact with the polycrystalline sample. Target 2 had a double-skinned "dummy" window (i.e., two 25 μm titanium foils separated by a 1 mm gap) intended as a reference case not directly in contact with the powder but subjected to the same beam secondary thermal excitation. LDV targets 3 and 5 were, respectively, aimed at the 150 μm and at the 1 mm packed bed samples. LDV target 4 was aimed at a 150 μm packed bed sample also with a double dummy diaphragm to permit the effects of the interaction of the powder and secondary heating to be separated.

A series of PT100 platinum resistance thermistors were used to acquire the temperature on the titanium beam entry (upstream) and exit (downstream) windows, as well as the temperature at the bottom of the resettable aluminum trough. PT100 were also mounted on the heat sinks and used to monitor the temperature of the LED clusters. Two Keller PAA-23SY 0-5 bar(a) pressure transducers were used to record the pressure in the inner and outer containment boxes. These sensors typically tripped at beam impact and required a power cycle to return to measuring the pressure. The feed from the aforementioned supplementary instrumentation on the rig was acquired using a Graphtec GL800 multichannel data logger.

Figure 6 shows a record of beam induced heating in the resettable trough in contact with the tungsten powder. The measurements were logged from three thermistors placed on the upstream and downstream titanium windows (in contact with the powder) and underneath the bulk of the aluminum trough. The slow temperature decline is probably attributable to convection through the helium atmosphere and conduction through the enclosure.

IV. BEAM AND SIMULATIONS

The beam intensity ranged from 3×10^{10} to 3.1×10^{12} POT with a nominal 2 mm beam sigma [i.e., defined as root mean square (rms)].

The intensity of the extraction was evaluated using a beam intensity monitor installed in the HiRadMat beam line. A pick-up-type beam position monitor was placed upstream of the experimental target area, recording the coordinates of the beam spot. The beam profile was measured on the first day using a Beam Observation TV (BTV) screen and on the subsequent days with the wire

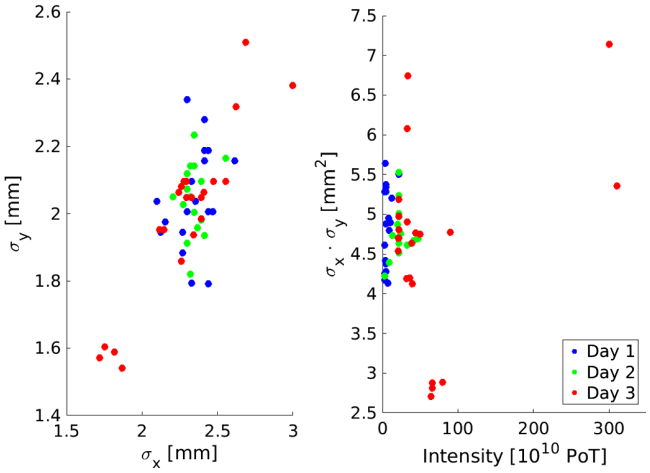

FIG. 7. Normalized beam parameters.

scanners of the Super Proton Synchrotron (SPS) at the point of the extraction. The beam profile readings from the three experimental sessions were normalized and are reported in Fig. 7, and a record of the beam parameters for each experiment is reported in Table II.

Figure 8 shows the radial energy deposition in a 50% v/v density tungsten powder sample as given by the Monte Carlo program FLUKA [14,15] assuming a 440 GeV/c, 2 mm sigma beam impinging on the powder from the right. Note that the expected peak temperature jump varied linearly with the POT and was of the order of 2000 K for the 3.1×10^{12} POT peak shot.

Figure 9 shows a FLUKA simulation of the residual charge in the tungsten powder immediately after a shot of 3.1×10^{12} POT. Note the positively charged regions on beam center line and at the powder surface. Note also

TABLE II. Beam parameters and extracted powder response.

Day	Run	σ_x [mm]	σ_y [mm]	Intensity POT	Beam depth from surf [mm]	Target sample	Max vel [m/s]	Max height [mm]	LDV target	Max LDV vel [m/s]	Max LDV disp [m]	Max vel delay [s]	Medium
1	1	NaN	NaN	NaN	6.9	NaN	0.00	0.0	NaN	0.000	0	0	Vacuum
1	2	NaN	NaN	NaN	NaN	NaN	0.00	0.0	NaN	0.000	0	0	Vacuum
1	3	2.44	2.19	4.4E+10	6.9	Sweep./p.beds	0.00	0.0	NaN	0.000	0	0	Vacuum
1	4	2.27	1.95	4E+10	7.0	Sweep./p.beds	0.13	2.1	3	0.030	3.90E−07	7.32E−05	Vacuum
1	5	2.15	1.98	3E+10	7.0	Sweep./p.beds	0.00	0.0	3	0.009	2.43E−07	8.79E−05	Vacuum
1	6	2.41	2.19	5E+10	7.1	Sweep./p.beds	0.17	2.1	3	0.031	5.00E−07	9.27E−05	Vacuum
1	7	2.1	2.04	4E+10	6.7	Sweep./p.beds	0.00	0.0	4	0.078	2.41E−06	1.61E−04	Vacuum
1	8	NaN	NaN	3E+10	6.8	Sweep./p.beds	0.00	0.0	4	0.092	1.59E−06	2.15E−04	Vacuum
1	9	2.27	1.88	4.3E+10	6.7	Sweep./p.beds	0.18	1.3	5	0.033	1.07E−07	1.42E−04	Vacuum
1	10	2.33	2.1	4.7E+10	7.3	Sweep./p.beds	0.17	1.9	5	0.077	3.20E−06	0	Vacuum
1	11	2.33	1.79	3E+10	4.6	Sweep./p.beds	0.13	0.5	5	0.041	1.16E−07	0	Vacuum
1	12	2.41	2.19	3E+10	4.6	Sweep./p.beds	0.09	0.9	5	0.060	8.85E−08	0	Vacuum
1	13	2.3	2.01	3E+10	4.6	Sweep./p.beds	0.18	2.3	5	0.066	7.94E−07	0	Vacuum
1	14	2.44	1.79	5E+10	4.5	Sweep./p.beds	0.22	2.7	4	0.075	4.01E−06	1.42E−04	Vacuum
1	15	NaN	NaN	5E+10	2.6	Sweep./p.beds	0.23	2.2	5	0.000	0	0	Vacuum
1	16	2.3	2.34	5E+10	2.6	Sweep./p.beds	0.15	2.1	5	0.094	3.17E−06	0	Vacuum
1	17	NaN	NaN	5.4E+10	1.5	Sweep./p.beds	0.06	0.3	5	0.000	0	0	Vacuum
1	18	2.61	2.16	4E+10	1.5	Sweep./p.beds	0.00	0.0	5	0.026	8.32E−08	0	Vacuum
1	19	NaN	NaN	8E+10	11.2	Sweep./p.beds	0.14	1.9	3	0.069	1.12E−06	4.40E−05	Vacuum
1	20	2.36	2.04	9E+10	6.8	Sweep./p.beds	0.35	8.3	4	0.130	3.50E−06	4.35E−04	Vacuum
1	21	2.13	1.94	7E+10	4.9	Sweep./p.beds	0.27	4.0	5	0.000	0	0	Vacuum
1	22	2.47	2.01	8E+10	5.1	Sweep./p.beds	0.30	6.4	3	0.087	7.23E−07	7.33E−05	Vacuum
1	23	NaN	NaN	1.2E+11	4.6	Sweep./p.beds	0.46	15.1	3	0.069	1.76E−06	1.22E−04	Vacuum
1	24	2.41	2.16	1.2E+11	4.7	Sweep./p.beds	0.40	11.7	3	0.000	0	0	Vacuum
1	25	2.44	2.01	1.1E+11	5.1	Sweep./p.beds	0.28	7.7	3	0.071	2.44E−06	4.88E−05	Vacuum
1	26	NaN	NaN	3.3E+11	4.8	Sweep./p.beds	1.85	43.5	3	0.000	0	0	Vacuum
1	27	2.41	2.28	2.2E+11	4.4	Sweep./p.beds	0.56	19.6	3	0.127	8.86E−06	2.83E−04	Vacuum
1	28	NaN	NaN	2E+11	4.6	Multisize	2.13	45	3	0.071	2.28E−06	−0.0181	Vacuum
2	1	NaN	NaN	NaN	NaN	NaN	0.00	0.0	NaN	0.000	0	0	Vacuum
2	2	NaN	NaN	NaN	NaN	NaN	0.00	0.0	NaN	0.000	0	0	Vacuum
2	3	NaN	NaN	NaN	NaN	NaN	0.00	0.0	NaN	0.000	0	0	Vacuum
2	4	2.32	1.82	3.4E+10	NaN	Mult-size	0.00	0.0	4	0.005	7.36E−07	6.35E−05	Vacuum
2	5	2.3	1.91	8.6E+10	NaN	Multisize	0.51	12.8	4	0.010	8.24E−07	0.000 161	Vacuum
2	6	2.3	2.07	*2.2E+11*	*9.9*	Sweep./p.beds	0.22	4.2	4	0.117	5.82E−06	0.000 527	Vacuum

(Table continued)

TABLE II. *(Continued)*

Day	Run	σ_x [mm]	σ_y [mm]	Intensity POT	Beam depth from surf [mm]	Target sample	Max vel [m/s]	Max height [mm]	LDV target	Max LDV vel [m/s]	Max LDV disp [m]	Max vel delay [s]	Medium
2	7	*2.3*	2.12	2.2E+11	*9.9*	Sweep./p.beds	0.63	15.7	4	0.120	9.91E−06	0.000 674	Vacuum
2	8	2.34	2.14	*2.2E+11*	8.6	Sweep./p.beds	0.31	5.2	4	0.235	6.93E−06	0.000 273	Vacuum
2	9	2.2	2.05	2.18E+11	6.5	Sweep./p.beds	0.36	5.3	4	0.127	2.73E−05	0.000 181	Vacuum
2	10	2.3	2.12	2E+11	4.6	Sweep./p.beds	0.41	7.6	4	0.222	1.14E−05	0.000 146	Vacuum
2	11	2.56	2.16	2.2E+11	2.5	Sweep./p.beds	0.58	9.1	4	0.253	5.37E−06	8.79E−05	Vacuum
2	12	2.39	2.1	2.2E+11	0.3	Sweep./p.beds	0.38	7.2	4	0.257	5.35E−06	0.000 112	Vacuum
2	13	2.34	2.23	2.2E+11	−0.6	Sweep./p.beds	0.26	2.4	4	0.240	1.75E−06	0.000 122	Vacuum
2	14	2.37	1.96	2.2E+11	−1.0	Sweep./p.beds	0.20	2.0	4	0.184	2.46E−06	8.30E−05	Vacuum
2	15	2.34	2	4.7E+10	5.1	Sweep./p.beds	0.00	0.0	5	0.025	1.88E−07	2.44E−05	Vacuum
2	16	2.41	1.93	4.15E+10	5.9	Sweep./p.beds	0.00	0.0	5	0.132	1.87E−06	0.000 21	Vacuum
2	17	2.39	1.98	1.33E+11	6.3	Sweep./p.beds	0.14	1.5	5	0.212	3.98E−06	0.000 356	Vacuum
2	18	2.32	2.14	2.19E+11	6.4	Sweep./p.beds	0.32	6.3	5	0.000	0	0	Vacuum
2	19	2.32	2.05	2.4E+11	6.5	Sweep./p.beds	0.33	6.9	5	0.275	5.29E−06	0.000771	Vacuum
2	20	2.27	2.03	3.3E+11	6.4	Sweep./p.beds	0.68	28.1	5	0.341	6.14E−06	2.98E−04	Vacuum
2	21	NaN	NaN	7E+11	6.0	NaN	0.00	0.0	3	0.000	0	0	Vacuum
2	22	NaN	NaN	*5E+11*	4.0	Sweep./p.beds	1.04	42.6	NaN	0.000	0	0	Vacuum
2	23	2.39	1.98	5E+11	4.0	Sweep./p.beds	0.83	32.7	3	0.216	3.20E−06	1.71E−04	Vacuum
2	24	2.28	2.1	9E+11	4.0	Sweep./p.beds	1.30	44.7	3	0.314	1.95E−05	2.93E−05	Vacuum
2	25	3	2.38	3E+12	4.4	Sweep./p.beds	5.30	44.8	3	0.436	6.93E−05	0.000 151	Vacuum
2	26	2.29	2.05	2.2E+11	8.7	Crystalline	4.83	42.9	1	0.282	1.74E−05	0.000 137	Vacuum
2	27	NaN	NaN	2.2E+11	8.7	Crystalline	0.58	16.8	1	0.000	0	0	Vacuum
2	28	2.26	2.08	2.1E+11	5.7	Crystalline	0.32	9.2	1	0.080	2.88E−06	3.42E−05	Vacuum
2	29	2.47	2.1	2.15E+11	5.7	Crystalline	0.00	0.0	1	0.000	0	0	helium
2	30	2.41	2.06	2.2E+11	10.0	Sweep./p.beds	0.12	1.3	3	0.339	3.78E−06	3.42E−05	Helium
2	31	2.29	2.1	2.2E+11	10.5	Sweep./p.beds	0.15	0.7	3	0.296	3.72E−06	3.91E−05	Helium
2	32	NaN	NaN	2.16E+11	13.0	Sweep./p.beds	0.17	0.5	3	0.336	2.91E−06	4.88E−05	Helium
2	33	2.34	1.94	2.05E+11	11.5	Sweep./p.beds	0.18	0.5	3	0.366	4.73E−05	5.37E−05	Helium
2	34	2.15	1.95	3.2E+11	7.3	Sweep./p.beds	0.30	3.9	3	0.402	4.41E−05	4.88E−05	Helium
2	35	2.26	1.86	3.6E+11	3.3	Sweep./p.beds	0.56	7.2	3	0.366	4.73E−05	5.37E−05	Helium
2	36	2.39	2.05	3.3E+11	4.5	Sweep./p.beds	0.40	3.4	3	0.332	1.77E−05	1.46E−05	Helium
2	37	2.33	2.05	4.4E+11	4.6	Sweep./p.beds	0.49	4.1	3	0.393	2.33E−05	1.76E−04	Helium
2	38	2.11	1.95	4E+11	5.0	Sweep./p.beds	0.36	3.2	3	0.402	1.88E−05	1.12E−04	Helium
2	39	2.25	2.06	3.9E+11	4.9	Sweep./p.beds	0.45	2.3	3	0.368	2.08E−05	2.34E−04	Helium
2	40	2.69	2.51	3.4E+11	2.3	Sweep./p.beds	0.37	3.7	3	0.360	1.09E−05	8.79E−05	Helium
2	41	NaN	NaN	3.8E+11	0.0	Sweep./p.beds	0.38	5.5	3	0.327	3.08E−06	3.42E−05	Helium
2	42	2.62	2.32	3.3E+11	6.0	Sweep./p.beds	0.38	3.6	3	0.363	1.10E−05	5.37E−05	Helium
2	43	2.56	2.1	3.1E+12	3.9	Sweep./p.beds	4.10	44.3	3	0.589	6.21E−05	0.000171	Helium
2	44	1.87	1.54	6.6E+11	3.6	Sweep./p.beds	0.68	5.9	3	0.000	0	0	Helium
2	45	1.75	1.6	6.6E+11	8.1	Sweep./p.beds	0.82	14.9	NaN	0.000	0	0	Helium
2	46	1.72	1.57	6.4E+11	6.3	Sweep./p.beds	0.62	8.6	NaN	0.000	0	0	Helium
2	47	1.82	1.59	8E + 11	2.6	Sweep./p.beds	0.98	15.2	NaN	0.000	0	0	Helium
2	48	*1.82*	*1.59*	8.1E+11	1.0	Sweep./p.beds	1.41	30.2	NaN	0.000	0	0	Helium
2	49	*1.82*	*1.59*	8.4E+11	−0.4	Sweep./p.beds	1.19	25.4	NaN	0.000	0	0	Helium
2	50	*1.82*	*1.59*	8.5E+11	−1.9	Sweep./p.beds	0.38	2.3	NaN	0.000	0	0	Helium
2	51	*1.82*	*1.59*	3.1E+12	3.9	Multisize	12.69	44.3	NaN	0.000	0	0	Helium

Italics indicates a missing or reconstructed parameter.

the annular negatively charged ring surrounding the beam core.

V. RESULTS

High-speed video footage recorded during the experiments revealed that the powder lifts both in a vacuum and in a helium atmosphere in response to the proton beam with a threshold intensity of approximately 3×10^{10} POT for 45 μm diameter tungsten spheres. This is a very similar threshold to that reported for sub-250 μm mixed tungsten powder reported in the previous experiment [11]. The lift velocity appears to be proportional to the beam intensity and varies along the 16 cm field of view of the camera.

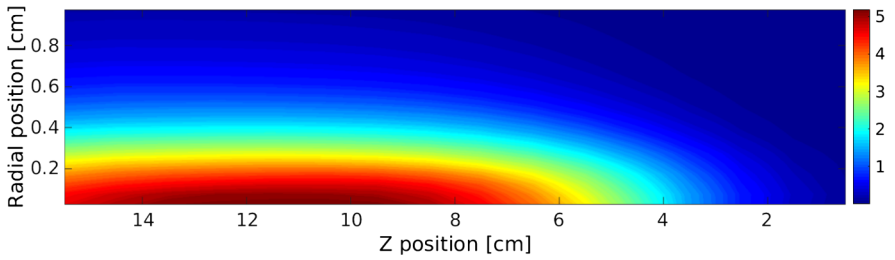

FIG. 8. Predicted energy deposition in tungsten powder (50% v/v) using an axisymmetric FLUKA model of a 10 mm radius cylinder. Results plotted in GeV/(cc primary).

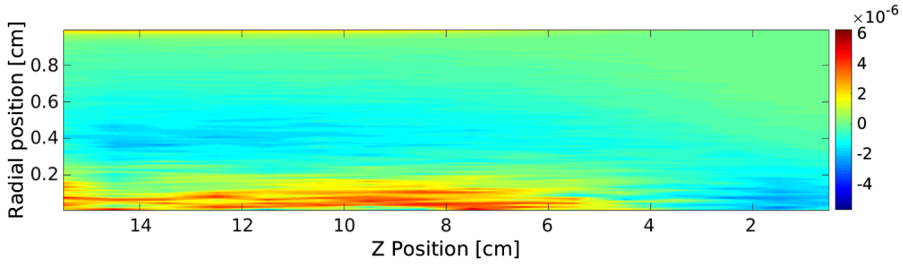

FIG. 9. Radial profile of the residual charge in a 10 mm radius 50% v/v tungsten cylinder for 3.1×10^{12} POT, calculated by FLUKA using an axisymmetric model. Results are plotted in C/cc.

Within this length, a maximum is generally identifiable, the location of which also appears to vary with the beam intensity [12]. The first half of the experiments was performed with the tungsten samples in a mechanical vacuum of ~20 mbar absolute pressure. The HSV image experiments were analyzed by logging the height of the powder lift as a function of the time around the longitudinal coordinate of maximum lift. The three HSV frames in Fig. 10 show the powder lift from a typical medium intensity shot (i.e., 2.2×10^{11} POT for the experiment designated as R1-27) with the beam impinging from the right-hand side. The images were extracted at, respectively, the beam impact and 25 and 71 ms after the beam impact (i.e., showing the peak lift). The images show evidence of powder caking against the container's glass walls and a free powder front (darker area at the top of the wave) separating from the bulk of the lift. Note in Fig. 10 that some dust initially adhering to the glass pane above the sweeper line was released at the beam impact and appears to be falling on the second frame.

Figure 11 shows the normalized lift data logged from experiment R1-27. The black dots on the left-hand plot show the height of the powder front (at the longitudinal coordinate of maximum lift), a polynomial fit to the data (in green), and a velocity (in red) derived from the fit. The graph on the right shows the interpolated lift (black line) and the ballistic trajectory which the powder would have followed if propelled by the initial measured velocity (blue line). The green and red lines are also ballistic trajectories calculated using an initial velocity measured at 0.04 and 0.082 s, respectively. Note that the measured powder expansion (black line) continues lifting past the ballistic trajectories, indicating that a lifting force is acting throughout the lift in addition to gravity. Even during the descent, the powder falls slower than expected under gravity, again suggesting that the grains are subjected to a force field.

Figure 12 shows the powder front velocity calculated from the results (blue line) compared with that of a ballistic particle under gravity (green line). A value of acceleration is then calculated from the extracted velocity. The red line shows the difference between the calculated acceleration and that of a ballistic particle solely under the force of gravity. The positive value of net acceleration (red line) quantifies the upwards force field, which appears evident throughout most of the lift and which decreases as the powder lifts and then increases again as the powder falls.

Figure 13 reports the maximum lift velocity as a function of the beam intensity with the powder in a vacuum first and then in helium. A linear fit through the data indicates a factor of 1.3 higher response in a vacuum than in helium. This suggests that the helium atmosphere damped the powder bed expansion rather than contributing to it, a positive result since helium is likely to be a propellant for a powder-based target in future applications. This also shows that the aerodynamic effects were not dominant (although probably still present) within the experimental parameters.

Most of the experiments were performed with a nominal beam center 6 mm below the powder surface to ensure that most of the protons interacted with the powder. This corresponds to approximately 3 Gaussian sigmas for a nominal beam having $\sigma_x = \sigma_y \approx 2$ mm. Figure 14 shows the effect of varying the depth of the beam center on the

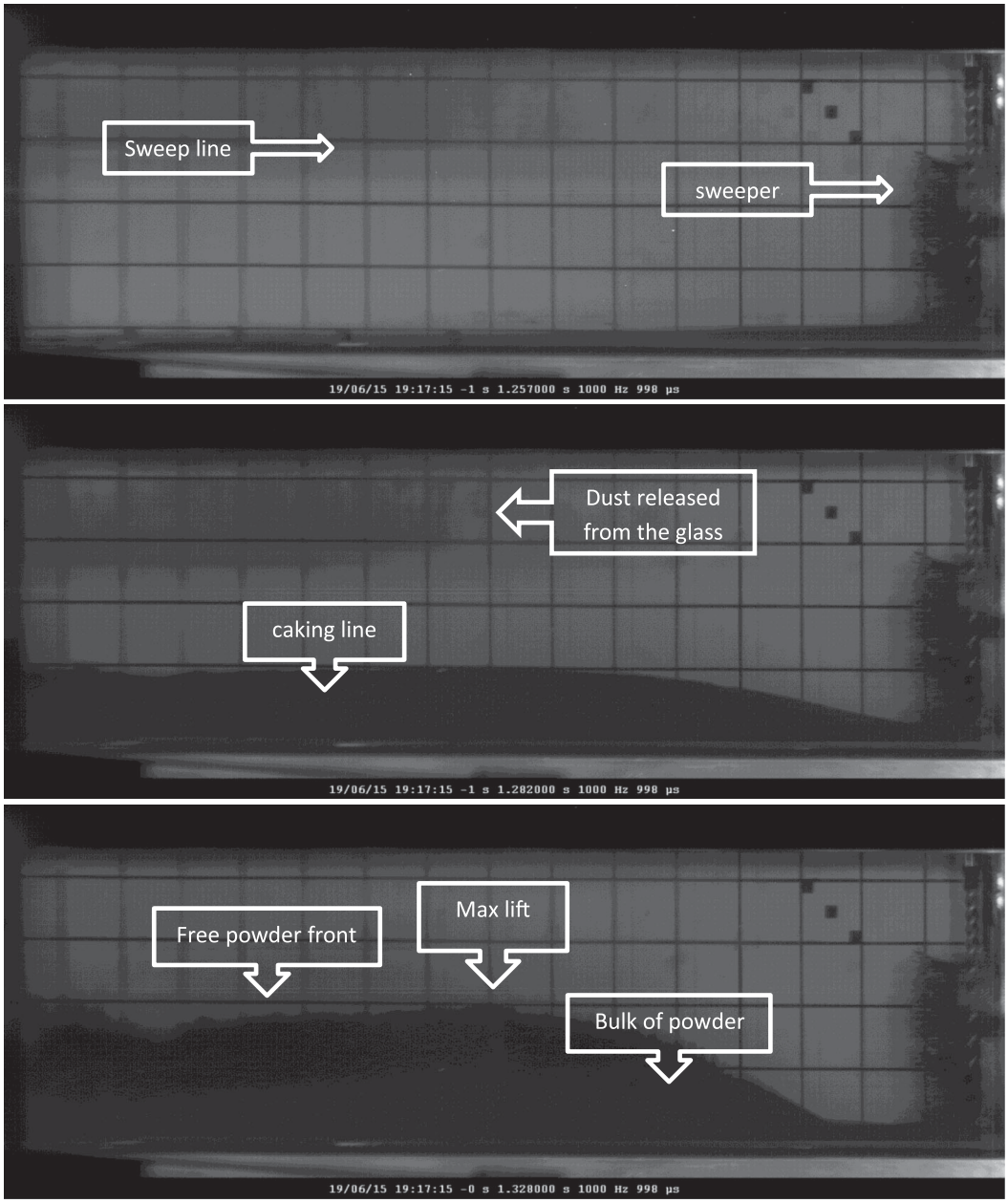

FIG. 10. High-speed video images of powder lift (R1-27), with the beam entering from the right.

peak lift velocity. The plot suggests a local maximum lift velocity occurring with a beam center around 3 mm below the powder surface. Shallower beams show a smaller response, probably due to the fewer protons and consequently smaller shower interacting with the tungsten. On the other hand, deeper beams had to lift a larger mass of tungsten, hence showing again a smaller response.

The results obtained in 2011 with a mixed crystalline powder in helium (triangles) are compared in Fig. 15 with a similar setup in 2015 in a vacuum (solid circles). Taking the 2011 data and scaling them linearly for higher POT (i.e., $2.2 \times 10^{11}/1.75 \times 10^{11} = 1.26$) gives the predicted lift shown by the hollow circles. The solid circles from the experiment in 2015 in a vacuum show a much greater response than expected from scaling the 2011 experiment in helium. A list of parameters comparing the setup of the two experiments is reported in Table III. It would appear that the mixed crystalline powder response is damped to a considerably greater extent by the helium environment than the factor of 1.3 observed in the 45 μm spherical powder.

In most experiments, a separation became visible during the lift where the free front of the powder separated from the bulk of the bed pressing or smearing against the glass sides of the trough. This phenomenon is evident in Fig. 10, and a typical lift data set (R1-26) is reported in Fig. 16. From the graph, it transpires that the free front proceeded at

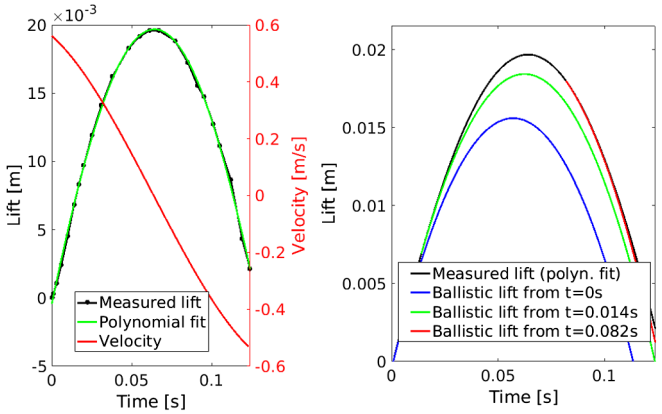

FIG. 11. Powder lift data, calculated velocity, and comparison to a ballistic trajectory (R1-27).

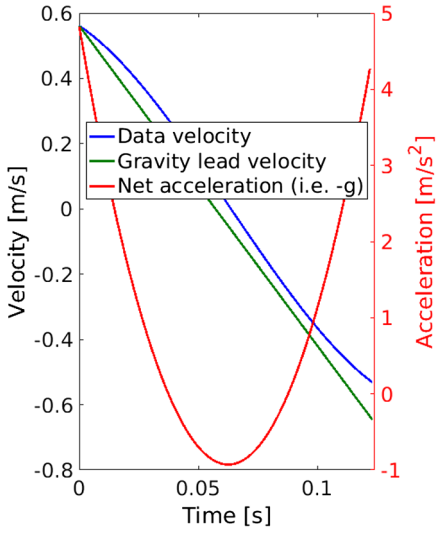

FIG. 12. Lift velocity and acceleration derived from the data (R1-27).

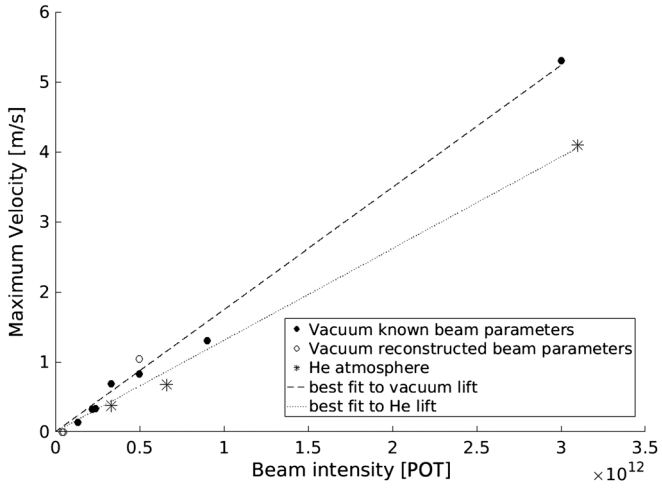

FIG. 13. Maximum lift velocity as a function of the beam intensity.

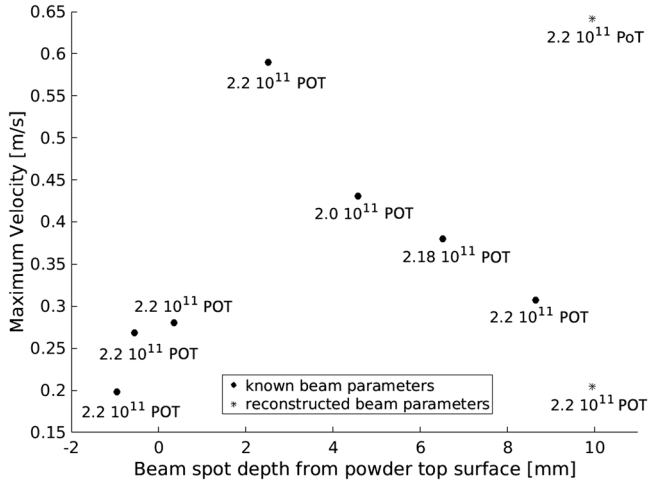

FIG. 14. Maximum lift velocity as a function of the beam depth.

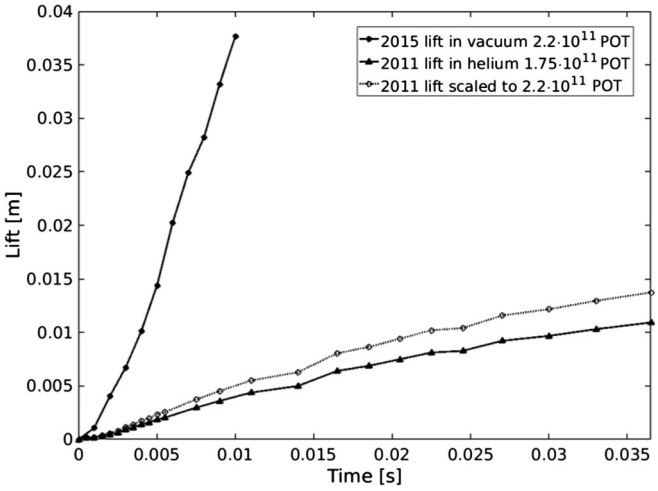

FIG. 15. Coarse mixed powder comparison to 2011.

a near constant speed, while the bulk of the bed slowed down, probably due to an interaction with the glass walls.

In several of the experiments, a secondary lift was detectable which seemed to be independent of the main powder bed expansion. Secondary lifts were in most cases limited in the longitudinal direction and often looked like bursting powder bubbles. Secondary lifts appeared randomly scattered in the longitudinal direction although always second to the primary eruption. Filamentation during the primary powder lift also appeared on a number of occasions. Figure 17 shows an example of the primary lift having reached its peak and descending with a filamented front while a secondary lift starts to rise and expand in the shape of a bubble.

Figure 18 shows the logged data from the primary and secondary lifts of experiment R1-19. Note how the two lifts have a comparable magnitude but appear independent of each other on both time and velocity.

TABLE III. 2011 and 2015 experiment parameter comparison.

Experiment	Powder	σ_x [mm]	σ_y [mm]	Intensity [POT]	Depth from surface [mm]	Trough type	Medium
R2-26 (2015)	<250 πm	2.29	2.05	2.21×10^{11}	8.68	Solid Al	Vacuum
N.8 (2011)	<250 πm	1.17	1.6	1.75×10^{11}	6	Sheet Ti	Helium

Figure 19 shows a high-speed video image of the multisized trough (middle trough in Fig. 3) irradiated with 2×10^{11} POT. The W-25 powder (furthest right in the image) produced the greatest response followed by proportionally smaller responses for the smaller grain sizes (W-45, W-90, and W-150). The 1 mm spheres did not appear to visibly lift. The experiment unequivocally revealed that smaller powder spheres responded to the beam with a higher lift and velocity than larger spheres.

The lift data from different size ranges are reported in Fig. 20, and Fig. 21 shows the lift velocity derived from polynomial fits to the lift data.

The analysis of high-speed video data from experiment R1-28 revealed a cloud of fines lifting from the far end of the trough (hardly visible on the far left in Fig. 19). Such a cloud might have originated from traces of fine powder resting either on the trough lip or among the 1 mm beads. A log of the trace of such fines along subsequent frames is reported in Fig. 22. Here each point from bottom right towards top left is separated by 1 ms. The fines clearly appear to lift upwards and subsequently change direction, flying towards the back of the trough. The leftward parabolic trajectory coincides in time with the lift of the bulk of the powder (on the right in Fig. 19), although no mechanical contact occurs between the fine cloud and the bulk of the powder. This suggests that the fines were subjected to a force field while in flight.

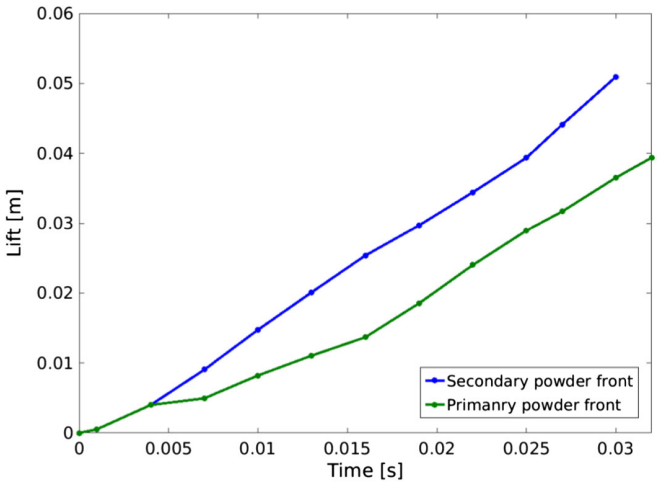

FIG. 16. Lift divergence. Record of run 1-26.

Analysis of the high-speed video data revealed an anomalous oscillation of the rig during high-intensity experiment R2-43 (3.1×10^{11} POT). In the video footage, the rig which was initially stationary seems to suddenly start to oscillate vertically. The green line in Fig. 23 reports the relative movement of the rig in the field of view. The oscillation starts around 20 ms after the beam impact and coincides with a luminescent event appearing at the back of the powder lift. In an attempt to identify whether the oscillation was due to an oscillation of the rig or of one of the optical mirrors returning the image to the HSV camera, a dust cloud was tracked falling inside the box. The red line in Fig. 23 shows the front of such a cloud as it falls through the field of view. The falling powder front displays a similar velocity pattern to that of the rig, suggesting that perhaps the movement was related to one of the optical elements rather than the powder-containing rig.

Figure 24 shows an image of the powder lift from experiment R2-43, 37 ms after a beam impact. Around this time, the lifting powder, which had been smearing against the glass wall, thins to the point where the lighter

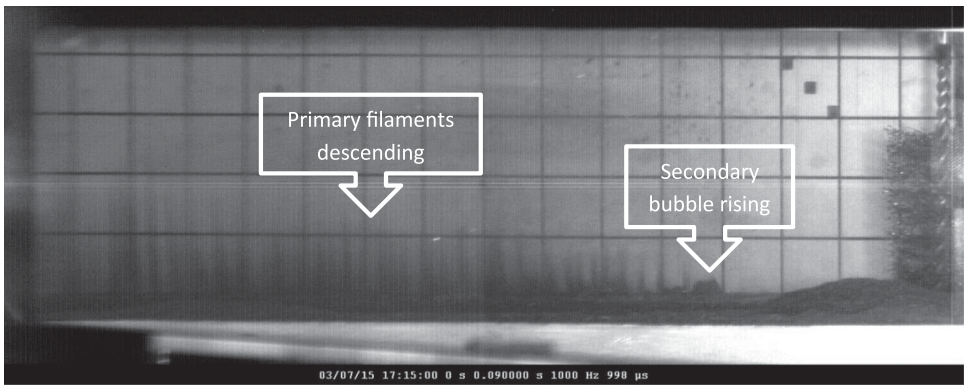

FIG. 17. Example of filamentation and secondary lift R2-37. The beam enters the sample from the right.

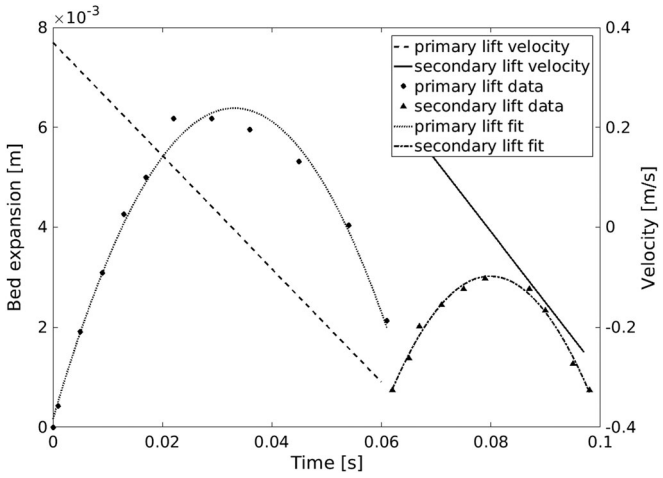

FIG. 18. Primary and secondary lift data R1-19.

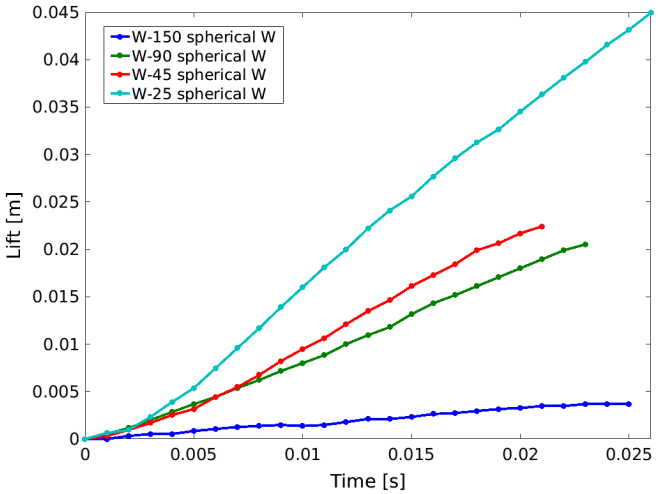

FIG. 20. Lift data from different powder sizes R1-28.

background is visible again. Note how some areas behind the lifting powder appear significantly lighter than the background, hence indicating a secondary flash.

Most of the experiments with a beam intensity sufficient to produce a lift exhibited some luminescence clearly identifiable in the first HSV frame at a beam impact. Figure 25 shows three HSV frames for high-intensity (3×10^{12} POT) experiment R2-25 extracted, respectively, 1 ms before the beam, at the beam impact, and 1 ms after the beam impact. Note the very bright area at the downstream end (left-hand side) above the trough in the beam impact frame. Note also the multitude of light speckles at and following the beam impact. The bottom right-hand corner of the last frame shows a magnified large speckle and a streak which appeared in experiment R1-24. Note that the large speckle is approximately 2 mm long, is made up of a multitude of pixels, and has two progressively dimmer but similarly shaped shadows which could be a reflection on the glass panes internal to the rig. The third frame in Fig. 25 is much darker than the one before the beam impact, consistent with radiation degradation of the LEDs and the optical windows as to be expected with a high-intensity shot.

The number and size of bright speckles in the beam impact frames appeared proportional to the beam intensity (compare Fig. 25 with Fig. 10). Figure 26 shows a quantitative analysis of such speckles as a function of the POT. The red triangles score the number of pixels in the perimeter of bright events using a "Canny Edge" function available in MATLAB, while the blue dots score the number of pixels in the areas of bright events selected via a binary threshold method.

The lighter speckles disappear sharply within the first few milliseconds of video footage. They could be the result of secondary radiation on the camera sensor: at least one isolated white pixel is identifiable recurring in several successive experiments. On the other hand, some of the speckles could be the result of electrostatic discharge in and around the rig. Large streaks and large shapes of odd morphology having dimmer reflections or shadows support this latter hypothesis.

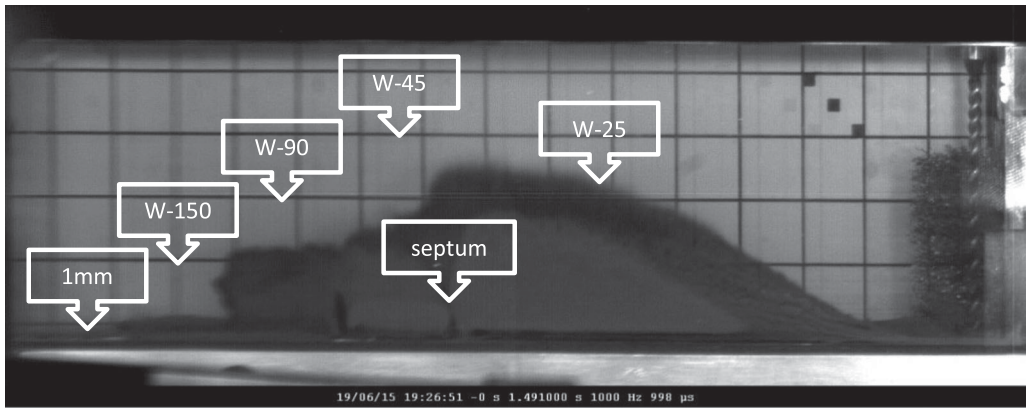

FIG. 19. Septa separated multisize experiment R1-28. 2×10^{11} POT. The beam impinges from the right.

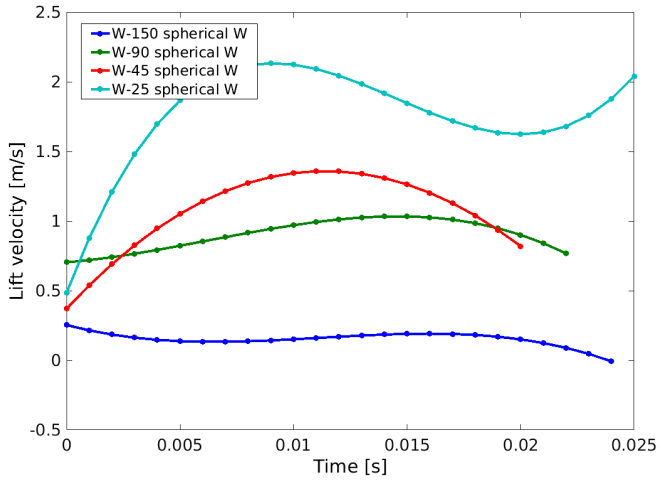

FIG. 21. Lift velocity of different powder sizes R1-28.

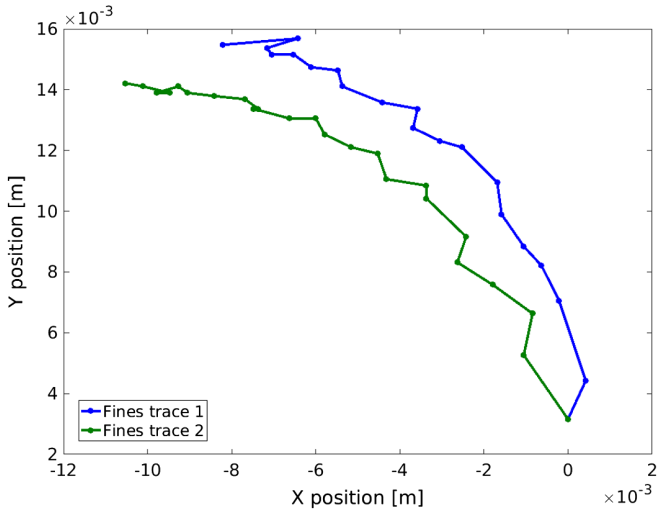

FIG. 22. Analysis of the trajectory of fine clouds from experiment R1-28.

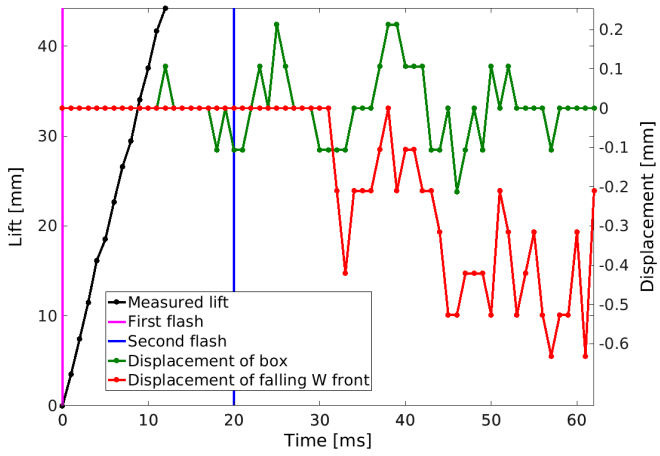

FIG. 23. Rig oscillation during high-intensity oscillation R2-43 (3.1×10^{12} POT).

VI. LASER DOPPLER VIBROMETER ANALYSIS

The free surface powder irradiation experiments were complemented by a set of enclosed samples. These samples had spherical grains arranged essentially as packed beds with thin titanium diaphragm windows. Two spherical samples with, respectively, 150 μm spheres and 1 mm spheres were complemented by a 150 μm sample with a dummy double window (i.e., with an outer titanium foil not in direct contact with the powder) intended to compare the beam induced thermal expansion of the window to that propagated by stresses in the grains. A LDV observed the titanium diaphragm at and following the beam impact.

With a view to measuring stress propagation within the media, the three packed bed samples and one of the free surface troughs were designed to have a thin titanium diaphragm in contact with the powder and observable with the LDV. The diaphragms were mounted at the same height as the beam nominal center and approximately 7 mm to the side of the beam path. Figure 27 shows three typical LDV signatures recorded on the three enclosed samples. Here the larger 1 mm spheres propagated a somewhat larger velocity when compared to the 150 μm spheres. However, the dummy window, not in contact with the powder, showed larger velocities than those in direct contact with the grains. This indicates that the dummy window is excited by secondary particles generated by the interaction of the proton beam with the powder samples. Since the windows in direct contact with the powder were observed to have a lower amplitude of vibration, notwithstanding being closer to the beam interaction point, then it would appear that the powder damps the initial vibration of the window or container resulting from the secondary particles.

Figure 28 shows a record of the peak velocities measured by LDV on the windows of the enclosed samples during the first day. In the graph, the points are colored by a normalized signal to noise ratio. The experiment clearly shows a relationship between the peak velocity and beam intensity. Note, however, that the following recordings were obtained having moved the rig and repositioned the LDV spot aiming for the center of the titanium diaphragms. So the large spread in measured velocities and displacements could be related to aiming at a slightly different spot within the titanium diaphragms.

Peak displacements were identified with the time restricted to the first 4 ms from the beam, and the time between the beam impact and the windows reaching their peak velocity value was scored. Figure 29 shows a record of peak displacements measured in this way by LDV on the windows of the enclosed samples during the first day of experiments. The average delay between the beam impact and peak velocity on 150 μm powder was 1.04×10^{-4} s, which assuming a distance of 7 mm results in a sound propagation speed in the powder of approximately 68 m/s. Such a sound speed is in line with off-beam benchtop

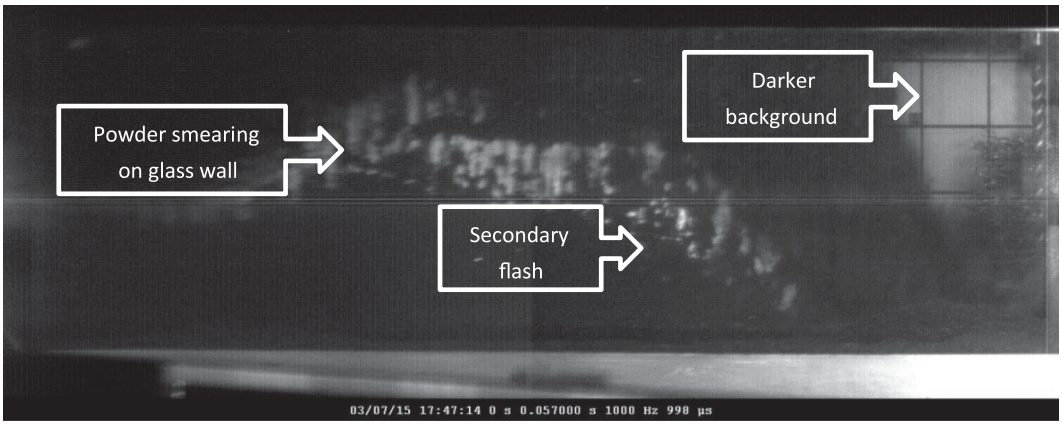

FIG. 24. Secondary flash appearing behind the lifting powder R2-43. The beam impinges the sample from the right.

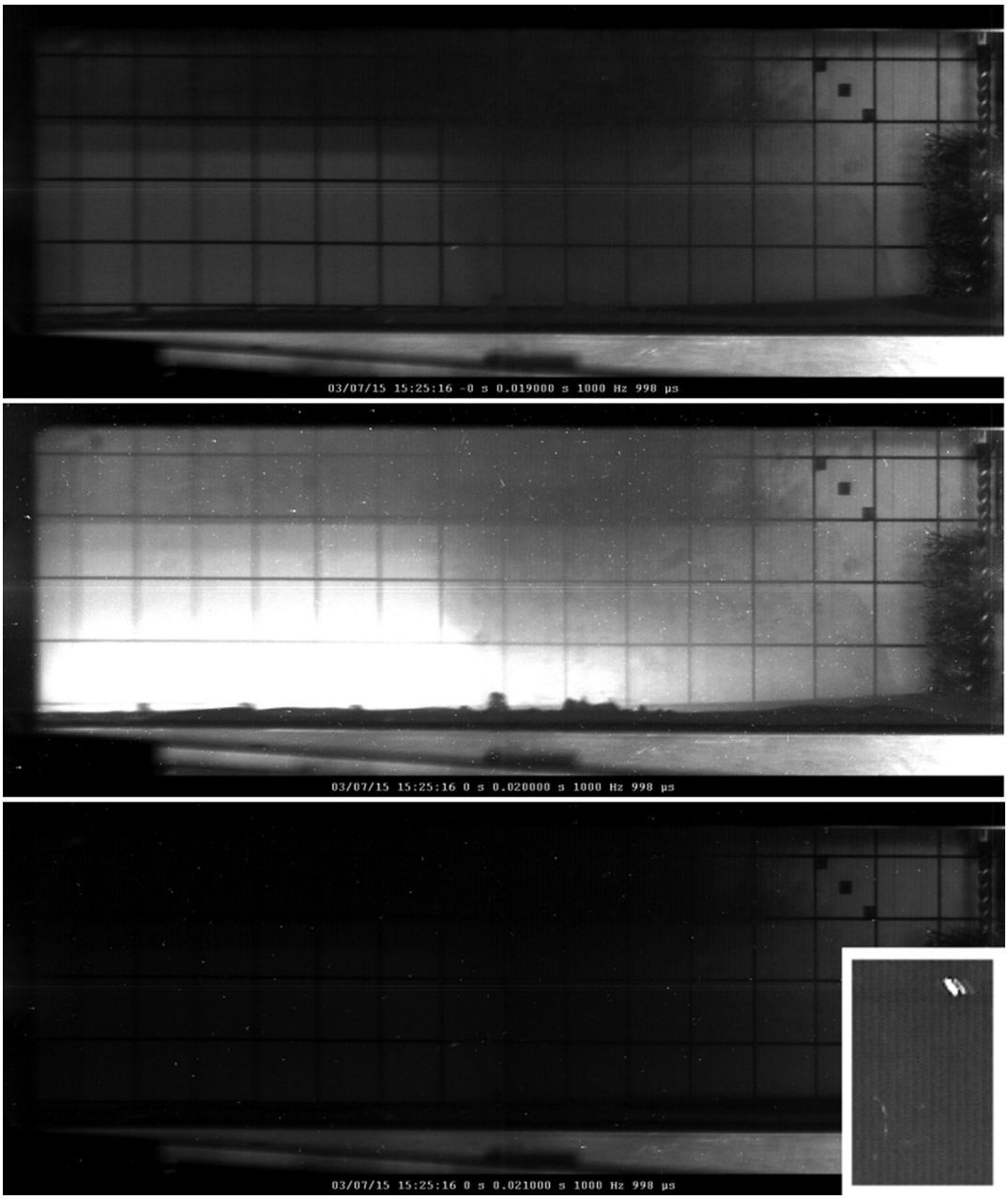

FIG. 25. Luminescent area and light speckles at beam impact R2-25 (3×10^{12} POT). The beam impinges the sample from the right.

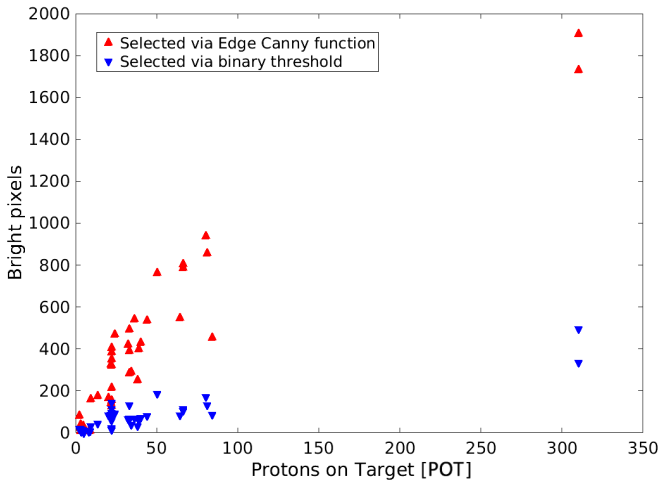

FIG. 26. Bright speckles recorded at the beam impact.

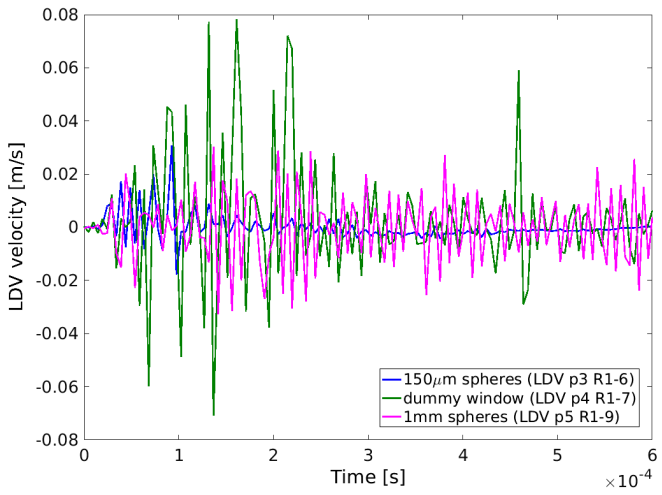

FIG. 27. LDV recorded window velocity signatures.

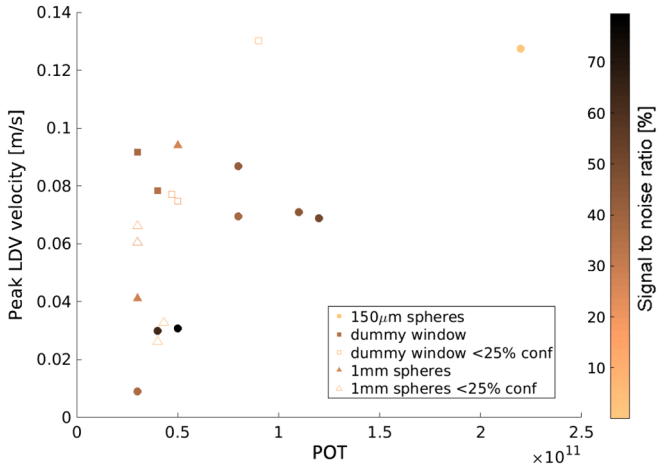

FIG. 28. Peak LDV velocities measured in day 1 as a function of the beam intensity.

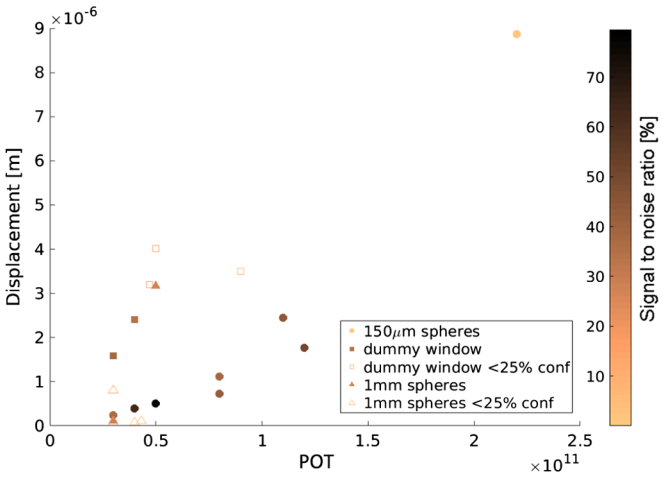

FIG. 29. Peak LDV displacements measured in day 1 as a function of the beam intensity.

experiments, which were performed using a piezo crystal to excite the powder.

VII. CONCLUSIONS

The experiment measured the response of granular tungsten samples of various sizes to a 440 GeV/c proton beam in vacuum and helium environments.

Powder lifts were observed in a vacuum, indicating a nonaerodynamic lift mechanism. A similar lift threshold was observed in atmospheric pressure helium, but with a slower response by a factor of around 1.3 for 45 μm tungsten spheres. The threshold intensity for a mechanical response in W-45 appeared to be around 3×10^{10} POT in a vacuum, and the peak lift velocities were of 5.3 m/s with 45 μm spheres at 3×10^{12} POT in a vacuum (corresponding to a peak energy density of 184.7 J/g) and 4.1 m/s at 3.1×10^{12} POT in helium. The initial acceleration in these lifts was of the order of 1000 m/s^2, since the initial velocities were observed after the first 1 ms HSV shutter interval.

Small diameter spheres showed a greater response than larger ones, and 1 mm beads did not appear to lift when irradiated. Considering that stress propagation through a granular medium is larger for larger grain sizes, it appears that, while thermal expansion driven stress propagation was probably present, it was not the dominant driver for the powder lifts. It is proposed here that electrostatic or electromagnetic effects on the grains following the transit of the beam played a key role in the powder lifts. This is reinforced by the observation that the powder appeared to continue lifting against gravity after the initial acceleration, suggesting that a force field was active on the powder for several tens of milliseconds after the beam impact. The powder response appeared smaller in helium than in a vacuum, suggesting that the gas reduced the force field acting on the grains.

HSV measurements of the open surface samples demonstrated that the maximum powder lift velocity was proportional to the impinging beam intensity.

Varying the beam depth with respect to the powder surface produced lifts of varying heights at an intensity of $\sim 2 \times 10^{11}$ POT, suggesting that the gravitational force acting on the powder bed had a similar order of magnitude to the lifting force.

The mixed crystalline sample tested showed a greater mechanical response to the beam than ~45 μm spherical samples. However, a comparison with the 2011 experiment in helium appears to show that the helium damps the response of the mixed crystalline material considerably more than was observed for the spherical grains.

LDV experiments showed that a thin titanium diaphragm in contact with a packed bed is excited by the grains at a beam impact, resulting in displacements of the order of ~ 0.5 μm for 0.5×10^{11} POT and ~ 9 μm for 2.2×10^{12} POT. The delay in the response of the diaphragm after a beam impact suggest that the sound propagation speed in 150 μm spheres is of the order of approximately 68 m/s. Peak velocities of around 0.13 m/s for 2.2×10^{11} POT measured by the LDV on the diaphragms suggest that stress induced velocities are smaller than the free surface expansion velocity of the bed (0.25 m/s for 150 μm spheres at 2×10^{11} POT).

Diffused luminescence was observed around the powder at a beam impact. Small, very bright areas in the HSV at a beam impact (and for the following few milliseconds) could be due to the interaction of radiation with the camera sensor or evidence of a static discharge in or around the powder.

ACKNOWLEDGMENTS

The authors thank the CERN HiRadMat and SPS operation teams for the technical support during the experiment. The research leading to these results has received partial funding from the European Commission and Science and Technology Facilities Council (STFC) under the FP7 Capacities project EuCARD2, Grant Agreement No. 312453. We also thank Dr. Lei Yang, Director of the Laboratory for Spallation Targets at IMPCAS, and Dr. Jiangfeng Wan, Leader of The Granular Target Design group, for supplying some of the tungsten material used for the experiments.

[1] C. J. Densham, O. Caretta, and P. Loveridge, in *Proceedings of the 23rd Particle Accelerator Conference, Vancouver, Canada, 2009* (IEEE, Piscataway, NJ, 2009), WE1GRC04.

[2] T. Davies, O. Caretta, C. Densham, and R. Woods, The production and anatomy of a tungsten powder jet, Powder Technol. **201**, 296 (2010).

[3] L. Yang and W. Zhan, New concept for ADS spallation target: Gravity-driven dense granular flow target, Sci. China: Technol. Sci. **58**, 1705 (2015).

[4] Interim Design Report No. IDS-NF-020, International Design Study for the Neutrino Factory, 2011.

[5] O. Caretta, T. Davenne, P. Loveridge, and C. J. Densham, Engineering considerations on targets for a neutrino factory and muon collider, J. Nucl. Mater. **433**, 538 (2013).

[6] J. Lettry, A. Fabich, S. Gilardoni, M. Benedikt, M. Farhat, and E. Robert, Thermal shocks and magnetohydrodynamics in high power mercury jet targets, J. Phys. G **29**, 1621 (2003).

[7] A. Fabich, M. Benedikt, and J. Lettry, Experimental observation of proton-induced shocks in free surface liquid metal targets, J. Nucl. Mater. **318**, 109 (2003).

[8] B. W. Riemer, M. W. Wendel, D. K. Felde, A. A. Abdou, and D. A. McClintock, Status of R&D on mitigating the effects of pressure waves for the Spallation Neutron Source mercury target, J. Nucl. Mater. **431**, 160 (2012).

[9] H. Kogawa *et al.*, Effect of proton beam profile on stress in JSNS target vessel, J. Nucl. Mater. **343**, 178 (2005).

[10] I. Efthymiopoulos, in *Proceedings of the AMAT Workshop at CERN, 2013*.

[11] O. Caretta, T. Davenne, C. Densham, M. Fitton, P. Loveridge, J. O'Dell, N. Charitonidis, I. Efthymiopoulos, A. Fabich, and L. Rivkin, Response of a tungsten powder target to an incident high energy proton beam, Phys. Rev. ST Accel. Beams **17**, 101005 (2014).

[12] N. Charitonidis, Design optimisation of a high intensity beam facility and feasibility experiment of a solid fragmented target, CERN-THESIS-2014-067, http://inspirehep.net/record/1339906?ln=en.

[13] M. Glor, Hazards due to electrostatic charging of powders, J. Electrost. **16**, 175 (1985).

[14] A. Fasso, A. Ferrari, J. Ranft, and P. Sala, Reports No. CERN-2005-10, No. INFN/TC_05/11, and No. SLAC-R-773, 2005.

[15] T. T. Böhlen, F. Cerutti, M. P. W. Chin, A. Fassò, A. Ferrari, P. G. Ortega, A. Mairani, P. R. Sala, G. Smirnov, and V. Vlachoudis, The FLUKA code: Developments and challenges for high energy and medical applications, Nucl. Data Sheets **120**, 211 (2014).